



**HAL**  
open science

## Simulations of high-velocity impacts on metal in preparation for the Psyche mission

Clara Maurel, Patrick Michel, J. M. Owen, Richard P. Binzel, M. Bruck Syal, G. Libourel

► **To cite this version:**

Clara Maurel, Patrick Michel, J. M. Owen, Richard P. Binzel, M. Bruck Syal, et al.. Simulations of high-velocity impacts on metal in preparation for the Psyche mission. *Icarus*, 2020, 338, pp.113505. 10.1016/j.icarus.2019.113505 . hal-02432546

**HAL Id: hal-02432546**

**<https://hal.science/hal-02432546>**

Submitted on 22 Dec 2020

**HAL** is a multi-disciplinary open access archive for the deposit and dissemination of scientific research documents, whether they are published or not. The documents may come from teaching and research institutions in France or abroad, or from public or private research centers.

L'archive ouverte pluridisciplinaire **HAL**, est destinée au dépôt et à la diffusion de documents scientifiques de niveau recherche, publiés ou non, émanant des établissements d'enseignement et de recherche français ou étrangers, des laboratoires publics ou privés.

1 **Simulations of high-velocity impacts on metal in preparation for the**

2 **Psyche mission**

3

4 Clara Maurel<sup>1</sup>, Patrick Michel<sup>2</sup>, J. Michael Owen<sup>3</sup>, Richard P. Binzel<sup>1</sup>, Megan Bruck-Syal<sup>3</sup>, G.

5 Libourel<sup>2</sup>

6

7 <sup>1</sup> Department of Earth, Atmospheric and Planetary Sciences, Massachusetts Institute of

8 Technology, Cambridge, MA 02139, USA

9 <sup>2</sup> Université Côte d'Azur, Observatoire de la Côte d'Azur, CNRS, Laboratoire Lagrange, CS

10 34229, 06304 Nice Cedex 4, France

11 <sup>3</sup> Lawrence Livermore National Laboratory, Livermore, CA 94551, USA

12

13 **Abstract**

14 In 2026, the NASA Discovery mission Psyche will orbit the asteroid (16) Psyche, the largest known

15 metal-rich asteroid in the main belt. To estimate relative ages of the surface, identify re-surfacing

16 events and better constrain Psyche's history, impact craters will be counted and characterized. No

17 spacecraft has ever visited a metal-rich small body; therefore, laboratory-scale impact experiments

18 and numerical simulations will play an important role in the interpretation of the mission's data.

19 However, the planetary applications of high-velocity impacts have so far mostly been studied for

20 silicate targets. Limited attention has been drawn to planetary objects predominantly made of

21 metal, and more laboratory experiments and numerical calibrations are needed. As part of this

22 effort, we present a suite of numerical simulations using an adaptative smoothed particles

23 hydrodynamics numerical code (ASPH) reproducing a high-velocity impact experiment conducted  
24 on a steel target. This work primarily focuses on the influence of the chosen equation of state and  
25 initial distribution of flaws in the material on the estimated crater dimensions, damage and  
26 temperature. We find that changing the EOS and initial flaw distribution affects the crater  
27 dimensions, though for a vast majority of cases the dimensions remain within 20% of the  
28 experimental values. The target is in most cases only locally weakened but not fully damaged,  
29 independently from the EOS chosen. Finally, temperatures at the impact point and around the  
30 forming crater can reach values above the melting point of iron at  $< 100$  GPa, which is in agreement  
31 with experimental observations. These results allow us to speculate on the differences expected  
32 between the surfaces of visited silicate-rich asteroids and that of the metal-rich target of the Psyche  
33 mission.

34

## 35 **1. Introduction**

36 In 2026, the NASA Discovery mission Psyche will orbit the  $\sim 200$ -km asteroid (16) Psyche (Elkins-  
37 Tanton et al., 2017). The asteroid bulk density estimate of  $3990 \pm 260$  kg m<sup>-3</sup> (Viikinkoski et al.,  
38 2018) is consistent with that of stony-iron meteorites. The high radar albedo of Psyche ( $0.37 \pm$   
39  $0.09$ ) also strongly suggests the presence of metal in abundance at its surface (Shepard et al., 2017).  
40 This makes Psyche the largest known metal-rich asteroid in the main belt. The leading hypothesis  
41 to explain the nature of Psyche is that the asteroid is the metallic core of an ancient planetesimal,  
42 whose silicate mantle was stripped away by one or several grazing, hit-and-run impacts (Asphaug  
43 and Reufer, 2014). This idea remains challenged, for example, by the possibility that Psyche  
44 accreted from a metal-rich reservoir in the proto-planetary disk (Weisberg et al., 2010).

45           The instruments on board the spacecraft will use different approaches to constrain the  
46 history of the asteroid, with the objective to elucidate Psyche’s nature. One of these approaches is  
47 to count and characterize impact craters. The recent radar-derived shape model of Psyche has  
48 already allowed the identification of two large depressions in the topography of the asteroid,  
49 interpreted as being two craters larger than ~20 km in diameter (Shepard et al., 2017). Although  
50 unresolved by this shape model, it is expected that hundreds of > 100-m craters will be observed  
51 over the course of the mission based on collisional evolution models of the main belt (Marchi et  
52 al., 2019). Craters on small bodies and planets constitute an important source of information to  
53 estimate 1) the age of the asteroid relative to other planetary bodies, 2) the chronology of events  
54 that shaped the asteroid, 3) the environment in which the body evolved and 4) the composition and  
55 strength of its subsurface.

56           Psyche poses an additional challenge compared to other small and planetary bodies studied  
57 *in situ* since no spacecraft has ever visited a metallic asteroid. Also, most numerical and small-  
58 scale experimental studies of planetary impacts have been carried out on silicates. Since both the  
59 size and shape of craters are affected by the nature of the asteroid’s surface (Jutzi et al., 2015;  
60 Marchi et al., 2016), calibrations against well-known crater size distributions may not apply  
61 optimally to Psyche. An important effort in understanding cratering processes in metallic material,  
62 through a combination of impact experiments and simulations, is therefore crucial for the  
63 interpretation of the mission’s data.

64           For decades, industrial and military applications of high-velocity impacts on metals  
65 provided data for the development of several strength models and equations of state (Steinberg et  
66 al., 1980; Johnson and Cook, 1985; Tillotson, 1962; Thompson and Lauson, 1972). Although  
67 limited attention has been drawn to the planetary-scale applications of high-velocity impacts on  
68 such materials, some impact experiments have been carried out on iron meteorites—possible

69 analog to Psyche’s surface—or alloyed irons with comparable mechanical properties (Matsui et al.,  
70 1984; Katsura et al., 2011; Ogawa et al., 2017; Ganino et al., 2018; Libourel et al., 2019; Marchi  
71 et al., 2019).

72 For example, Ganino et al. (2018) and Libourel et al. (2019) carried out a suite of impact  
73 experiments on Cr–Mo alloy steel (SCM 435) and the iron meteorite Gibeon at the Institute of  
74 Space and Astronautical Science (ISAS) in Japan. The objective of the present study is to calibrate  
75 the adaptive smoothed particle hydrodynamics (ASPH) computational package Spheral++ (Owen  
76 et al., 1998) against the high-velocity impact experiments carried out by these authors. Relying on  
77 the well-established Steinberg-Guinan strength model for steel (Steinberg et al., 1980) we are  
78 interested in understanding the effect on crater dimensions of 1) the equation of state (EOS), and  
79 2) the dynamic fracture model (initial distribution of flaws in the material). We compare the  
80 outcomes of 86 simulations obtained with the Tillotson EOS (Tillotson, 1962) and ANEOS  
81 (Thomson and Lauson, 1972) with the same initial conditions using different initial flaw  
82 distributions characterized by a pair of Weibull parameters, with the objective to identify those that  
83 best fit the experimental data. We also compare the damage caused to the target in all cases, and in  
84 selected simulations we analyze the evolution of the target’s temperature.

85

## 86 **2. Numerical framework**

87 We use the computational package Spheral++, which employs the adaptative smooth-particle  
88 hydrodynamics method (ASPH; Shapiro et al., 1996; Owen et al., 1998). ASPH replaces the scalar  
89 smoothing scale of SPH (Monaghan, 1992) with a symmetric tensor, such that the resolution around  
90 each point is represented by an arbitrary ellipsoidal volume allowed to follow the local anisotropies  
91 in the particle distribution. This improves the locally Lagrangian approximation of ASPH in that

92 each material points volume can follow the Lagrangian deformation of the local fluid element more  
93 faithfully than the simple volume adaptation of SPH. The SPH smoothing scale approximation is  
94 really only appropriate for locally isotropic volume changes. In practice it means that ASPH allows  
95 the local resolution scale to follow while point distributions are stretched or compressed  
96 anisotropically. That way, both numerical stability as well as efficiency can be improved when  
97 resolution is needed in preferential directions. More details about Spheral++ can be found in the  
98 literature (Owen et al., 1998; Owen, 2004; Owen, 2014); here we describe the parameters and  
99 models used and investigated in our simulations. These include the equation of state (material-  
100 dependent equation that relates the pressure to the density and either directly the temperature or the  
101 internal energy), the strength model (which takes into account the mechanical reaction and the  
102 possible plastic deformations of the material) and the damage model (initial distribution of incipient  
103 flaws that may evolve in fractures under a given amount of stress).

104

## 105 **2.1. Equations of state**

106 The equation of state (EOS) relates the pressure of a system to its density and temperature or  
107 internal energy. This equation must be added to the equations of conservation and motion for a  
108 complete characterization of the system's dynamics. It is material-dependent, and typically consists  
109 in a set of interpolation parameters derived to match experimental data in the range of pressure,  
110 temperature and density of interest. The effect of two different equations of state is examined in  
111 this study: the Tillotson EOS (Tillotson, 1962) and ANEOS (Thomson and Lauson, 1972).

112 The Tillotson parameters for pure iron have been published by Melosh (1989) and are  
113 implemented as default values for iron in Spheral++. The main parameters for steel have also been  
114 published (Nesterenko, 2001). Both sets of parameters (Table 1) were compared by conducting two  
115 otherwise identical simulations, and no fundamental difference was found between the evolution

116 in time of the crater's dimensions (Fig. 1). Therefore, we chose to perform the rest of the  
117 simulations using the Tillotson parameters for pure iron, since they have been more widely used  
118 and the other EOS studied (ANEOS) has only been parameterized for pure iron.

119 No detailed work has recently been published on the ANEOS of pure iron since the original  
120 publications, unlike for example SiO<sub>2</sub> (Melosh, 2007). Two versions of ANEOS are available for  
121 pure iron, accounting for different phases and phase transitions (Melosh, private communication).  
122 The version adapted from the original ANEOS library matches experimental data for the solid-  
123 solid phase transition at ~13 GPa. This version, however, lacks a distinct liquid phase. Another  
124 version accounts for the liquid phase but not the solid-solid transition (Thompson, 1990); recent  
125 experimental work has shown the limitation of this version for very high pressures (~500 GPa;  
126 Kraus et al., 2015). Both versions of ANEOS would equally benefit from being re-evaluated in the  
127 light of new available experimental data.

128 The approximate pressure expected in the target during the compression phase of an impact  
129 was derived by Mizutani et al. (1990):

130

$$P \sim P_0 \left( \frac{D_P}{r} \right)^3 \quad (1)$$

131

132 where the initial peak pressure  $P_0$  is defined as:

133

$$P_0 \sim \frac{\rho_{0,t} C_t v \zeta}{2} \left( 1 + \frac{v S_t \zeta}{2 C_t} \right) \text{ where } \zeta = 2 \left[ 1 + \left( \frac{\rho_{0,t} C_t}{\rho_{0,p} C_p} \right)^{1/2} \right]^{-1} \quad (2)$$

134

135 In eqs. (1) and (2), subscripts  $t$  and  $p$  denote target- and projectile-related quantities.  $D_p$  (m) is the  
136 impactor diameter,  $r$  (m) is the distance from the closest point located on the sphere of radius  $D_p$   
137 below the impact point,  $\rho_0$  ( $\text{kg m}^{-3}$ ) is the initial density,  $C$  ( $\text{m s}^{-1}$ ) is the bulk sound velocity in the  
138 material,  $v$  ( $\text{m s}^{-1}$ ) is the impact velocity,  $s$  is a constant equal to 1.92 (Mizutani et al., 1990). Using  
139 eqs. (1) and (2), initial densities of 2700 and 7800  $\text{kg m}^{-3}$ , bulk sound velocity of 3500 and 5200  $\text{m}$   
140  $\text{s}^{-1}$  for basalt and iron, respectively, we find a peak pressure of  $\sim 75$  GPa and up to  $\sim 45$  GPa at 0.45  
141 cm below the crater (i.e., the depth of the final crater, see section 4). Given that the pressure  
142 involved in the area of interest during the impact can be much higher than 13 GPa, and that based  
143 on the experiments partial melting of the target is expected, we chose the version of ANEOS  
144 accounting for a liquid phase to compare to the suite of simulations carried out with the Tillotson  
145 EOS.

146

## 147 **2.2. Strength model**

148 The response of a system to an applied force strongly depends on the strength model implemented  
149 and it is crucial to choose the model most adapted to the simulated material. The Steinberg-Guinan  
150 strength model (Steinberg et al., 1980) describes the evolution of both the shear modulus and yield  
151 strength as a function of temperature, pressure and density—as opposed to the Johnson-Cook  
152 strength model, also commonly adopted for metals, which does only provide the yield strength.  
153 This model assumes that both shear modulus and yield strength are independent from the strain  
154 rate, which is only valid if the strain rate is higher than  $\sim 10^5 \text{ s}^{-1}$ . During an impact, the compressive  
155 strain rate  $\dot{\epsilon}$  is approximately:

156

$$\dot{\epsilon} \sim \frac{v_p r_p}{r^2} \quad (3)$$

157  
158 where  $v_p$  is the impact velocity,  $r_p$  the radius of the projectile and  $r$  is the distance (Melosh et al.  
159 1992). In our case, with  $v_p = 6.9 \text{ km s}^{-1}$ ,  $r_p = 1.9 \text{ mm}$  (Section 3) and  $r = 1 \text{ cm}$  (i.e.,  
160 approximatively twice the size of the final crater; Section 4.1), we find  $\dot{\epsilon} \sim 1.3 \times 10^5 \text{ s}^{-1}$ , which is  
161 above the model's validity threshold. The fitting parameters used for steel are summarized in Table  
162 2.

163

### 164 **2.3. Damage model**

165 The tensile stress applied during the impact yields the activation and propagation of flaws in the  
166 material, which irreversibly damage it (i.e., reduce its strength) up to an eventual breaking point.  
167 In Spheral++, the damage of a node is modeled by a tensor  $D$ , and the stress tensor applied to a  
168 node will be scaled down by  $I - D$ , where  $I$  is the identity matrix. Because the yield strength of a  
169 material is directly related to the stress applied by the Steinberg-Guinan model (Steinberg et al.  
170 1980), a damaged node will decrease in strength until it is fully damaged. It is then treated as a  
171 strengthless material. To quantify the damage of a node, we look at the maximum eigenvalue of  
172 the damage tensor calculated for this node.

173 The accumulation of damage in the material is modeled with the widely-used Grady-Kipp  
174 fragmentation theory (Grady and Kipp, 1980) adapted to SPH by Benz and Asphaug (1994). This  
175 theory relies on the existence of incipient flaws in the material—naturally occurring due to, for  
176 example, crystal defects. Each flaw possesses its own stress threshold above which it starts to grow  
177 in order to release part of the stress applied to the material. When the target is initialized, Spheral++  
178 distributes incipient flaws with different threshold stresses and assigns several flaws to each node.  
179 The distribution of these incipient flaws follows the Weibull statistics:

180

$$N(\sigma) = \left(\frac{\sigma}{\sigma_N}\right)^m \quad (4)$$

181

182 where  $N$  is the number of flaws that activate at or below a stress  $\sigma$  for a given volume. The  
183 parameters  $m$  and  $\sigma_N$  (called shape and scale parameters, respectively) are material dependent and  
184 can be experimentally determined—although so far a limited number of materials have been  
185 calibrated. Eq. (4) is also commonly found in the form  $n(\varepsilon) = k\varepsilon^m$ , where  $n$  is the number density  
186 of activated flaws at a strain  $\varepsilon$ , and:

187

$$k = \frac{1}{V} \left(\frac{E}{\sigma_N}\right)^m \quad (5)$$

188

189 where  $V$  and  $E$  are the volume and the Young's modulus of the target, respectively (Nakamura et  
190 al., 2007).

191 One objective of this study is to determine numerically the range of values of Weibull  
192 parameters  $m$  and  $\sigma_N$  (or equivalently  $k$ ) that best reproduce the impact experiment carried out by  
193 Ganino et al. (2018), and evaluate the dependence of the final crater dimensions on these  
194 parameters. None of them has been experimentally measured for SCM 435 steel, and no clear  
195 values of  $m$  and  $\sigma_N$  were identified in the literature for stainless steel. We selected the range of  
196 values investigated for  $\sigma_N$  using the fact that this parameter is related to the mean fracture stress  
197 ( $\bar{\sigma}$ ) of the material by:

198

$$\sigma_N \sim \frac{\bar{\sigma}}{\Gamma(1 + 1/m)} \quad (6)$$

199  
200 where  $\Gamma$  is the gamma function (Bergman, 1985). Taking  $\bar{\sigma}$  equal to the tensile strength of the SCM  
201 435 steel (since flaws activate in tension),  $\sigma_N$  should fall in the range 650–950 MPa for values of  
202 the shape parameter  $m$  between 2 and 30. Regarding an estimate of  $m$ , Asphaug et al. (2002)  
203 mention that metals could be approximated by  $m \sim 8$  (for reference, a value of 9.5 is often adopted  
204 for basalt). The authors do not provide additional information or reference. Accounting for the  
205 uncertainties of these parameters, we conducted a suite of simulations spanning a broad range of  
206 values of  $m$  (2, 5, 8, 10, 12, 15 and 30) and  $\sigma_N$  (0.05, 0.2, 0.5, 0.8, 0.9, 1.1, 1.5, 2.0 and 3.0 GPa).  
207 The equivalent values of the parameter  $k$  are given in Table 3.

208 Note that the Grady-Kipp fragmentation theory was developed to model failure in a brittle  
209 material, while steel and iron meteorites are both ductile at room temperature. However, Grady  
210 (2003) applied this theory to fragmentation of ductile metals explaining that although some stress  
211 may be accommodated by ductile deformation, this dissipation process is relatively limited and  
212 represents a minor contribution to the final outcome of high-strain rate events. Moreover, impact  
213 experiments comparing steel, Fe-Ni alloy and iron meteorites targets found no significant  
214 difference in crater shape between impacts above and below the brittle–ductile transition  
215 temperature (Matsui and Schultz, 1984; Libourel et al. 2019). Therefore, we assumed the Grady-  
216 Kipp theory could reasonably be applied to model high-velocity impacts in steel targets.

217

### 218 **3. Selected experiment**

219 We replicated a high-velocity impact experiment conducted by Ganino et al. (2018). In the  
220 experiment, the target was a cylinder of SCM 435 steel, with a diameter of 6 cm and a height of 3-

221 4 cm. In the simulation, the target is a parallelepiped of  $6 \times 6 \times 3$  cm. The projectile is a 80-mg  
222 sphere of basalt (i.e., with a radius of 1.92 mm, assuming a density of  $2700 \text{ kg m}^{-3}$ ) impacting  
223 vertically at  $6.89 \text{ km s}^{-1}$  under Earth gravity ( $9.81 \text{ m s}^{-2}$ ). It is initially located three radii above the  
224 target's surface (5.76 mm). The target is simulated with a resolution of 0.5 mm, which represents  
225  $\sim 866,000$  SPH particles. The impactor is made of  $\sim 93,800$  SPH particles; this number is calculated  
226 the mass per SPH particle is the same in the target and impactor. We also conducted two selected  
227 runs with a resolution of 0.2 mm to verify the convergence of the results with increasing resolution  
228 and also analyze the target's temperature. The SPH particles were assigned an EOS (Tillotson or  
229 ANEOS) and a strength according to the Steinberg-Guinan model for steel (Section 2.2). We  
230 carried out simulations with both EOS for 43 pairs of Weibull parameters  $m$  and  $\sigma_N$  (Section 2.3).  
231 We applied a plastic yield model with constant shear modulus  $G_0 = 22.7 \text{ GPa}$  and yield strength  
232  $Y_0 = 3.5 \text{ GPa}$  to characterize the projectile's strength and used Weibull parameters published for  
233 basalt ( $m = 9.5$  and  $k = 10^{30} \text{ cm}^{-3}$ ; Asphaug et al., 2002).

234

## 235 **4. Comparison with the impact experiment**

### 236 **4.1. Crater dimensions**

237 In the replicated experiment (Ganino et al., 2018), a crater diameter of 9.8 mm was measured at  
238 the original level of the target's surface and a depth of 4.5 mm was measured from this original  
239 level down to the bottom-center of the crater. We measured both quantities the same way at the  
240 end of the simulations (10  $\mu\text{s}$ ); at this time, all the craters had their final dimension. We considered  
241 the spatial resolution of our simulation (0.5 mm) as the uncertainty in the dimensions of the  
242 simulated craters; this corresponds to a 10% uncertainty for both diameter and depth.

243 With the Tillotson EOS, we find that only 58% of the diameters and 30% of the depths  
244 obtained in the simulations are within  $\pm 10\%$  of the experimental values, though all diameters and  
245 almost all depths (95%) remain within  $\pm 20\%$  (Fig. 2A). Both depth and diameter vary  
246 monotonically with the Weibull scale parameter  $\sigma_N$ : for a given shape parameter  $m$ , the dimensions  
247 decrease inversely to  $\sigma_N$  (except for  $m = 2$ , where they are approximately constant). In most cases,  
248 the higher  $\sigma_N$ , the closer the dimensions to experimental values. However, we do not observe  
249 significant differences when  $\sigma_N$  is kept constant and  $m$  varies. Both results are not surprising if we  
250 consider the cumulative distribution function of the Weibull distribution (Fig. 3). When  $\sigma_N$   
251 increases, a larger applied stress is necessary for the same amount of nodes to fail, yielding a  
252 smaller crater. If  $m$  increases, the simulated material becomes more homogenous, but the amount  
253 of stress needed to fail  $\sim 2/3$  of the nodes (definition of  $\sigma_N$ ) is the same, explaining why varying  $m$   
254 has less effect than  $\sigma_N$ . Interestingly, the pairs  $(m, \sigma_N) = (8, 0.8\text{--}0.9 \text{ GPa})$  are among the best fits  
255 when accounting for both diameter and depth. This is in agreement with our preliminary  
256 calculations for  $\sigma_N$  (Section 2.3), and with the value suggested by Asphaug et al. (2002) for  $m$ , and  
257 corresponds to a value of  $k$  of  $\sim 10^{17} \text{ cm}^{-3}$ .

258 With ANEOS, the diameters and depths are overall closer to experimental values with 77%  
259 and 51% within  $\pm 10\%$ , respectively (Fig. 2B). We observe a similar monotonic trend with  $\sigma_N$  as  
260 with the Tillotson EOS, with more spread in depth than diameter as a function of  $\sigma_N$ . Note that the  
261 pairs  $(m, \sigma_N) = (8, 0.8\text{--}0.9 \text{ GPa})$  also reproduce well the experimental values.

262

## 263 **4.2. Target damage**

264 Because the strength of a material decreases with accumulating damage, any area within the target  
265 with non-zero damage will be irreversibly and proportionally weakened. Ganino et al. (2018)

266 imaged a section of the crater with scanning electron microscopy (SEM) and observed  
267 deformations of the target and minor cracks within ~1 mm around the crater edge and up to several  
268 mm directly below the crater. Cracks < 0.2-mm wide were also observed down to about 2 mm  
269 underneath the bottom of the crater, indicating the material had marginally failed. Given the  
270 resolution of the nominal simulations (0.5 mm), it was expected that such cracks would not be  
271 resolved, but that a possible partial damage of the target could be found.

272 For  $m > 5$ , the cases where  $\sigma_N = 0.05$  GPa produce near-global failure of the target, with a  
273 majority of nodes damaged at 100%. This is also the case for  $m = 30$  and  $\sigma_N = 0.2$  GPa. The cases  
274 where  $m = 2$  leave the target completely undamaged. In all other cases and with both EOS, the first  
275 layer of SPH particles surrounding the crater is only partially damaged by the impact (Fig. 4A-B).  
276 Increasing  $m$  from 5 to 30 increases the maximum damage (typically near the impact point) of  
277 ~10% and the thickness of material damaged below the impact point by a factor of 2 to 3. Not  
278 surprisingly, increasing  $\sigma_N$  yields less damaged nodes because the average threshold stress of the  
279 incipient flaws shifts toward higher values. Globally, the smaller this scale parameter, the thicker  
280 and more damaged the layer of material below the crater. The Tillotson EOS yields on average a  
281 maximum that is about 10% smaller than the same simulation conducted with ANEOS. However,  
282 the EOS does not have a significant influence on the amount of damaged material below the crater  
283 (Fig. 4B). For the cases where the crater dimensions are within 10% the experimental values, the  
284 layer of damaged material below the crater does not exceed 2 mm, which is in agreement with  
285 experimental observations.

286 For comparison, we performed one simulation with the same initial setup, the Tillotson  
287 EOS and a basaltic target (Fig. 5A-B). We used the Weibull parameters of basalt ( $m = 9.5$ ,  
288  $k = 10^{30} \text{ cm}^{-3}$ ) and the strength model developed by Collins et al. (2004) for rock materials. The

289 impact resulted in a crater 1.5 times larger in diameter and depth after 10  $\mu\text{s}$  (end of the simulations  
290 with a steel target). We observed a more important damage (between 0 and 10%) affecting larger  
291 regions of the target, as opposed to the very localized, minor damage of the steel target. This  
292 illustrates the importance of the nature of the target in the characterization of impact craters.

293

### 294 **4.3. Temperatures in the target**

295 The temperature in the target was not measured during the experiments by Ganino et al. (2018).  
296 However, the authors found numerous metal beads embedded in the ejecta and in the quenched  
297 impactor melt that was deposited at the surface of the target or infiltrated in cracks, suggesting that  
298 the metal reached at least locally melting temperatures. Similarly, immiscible emulsion of silicate  
299 and Fe-Ni metal liquid were observed at the bottom of the crater on the Gibeon iron meteorite  
300 (Libourel et al., 2019), showing the target had experienced temperatures above the melting point  
301 of Fe-Ni metal.

302 We recorded the evolution of the temperature in the target for two simulations (one for each  
303 EOS) with 0.2-mm resolution and the Weibull parameters  $(m, \sigma_N) = (8, 0.9 \text{ GPa})$ . The Tillotson  
304 EOS relates the pressure and density to the internal energy of the system, not directly to the  
305 temperature, which is calculated assuming a constant specific heat capacity. Because of this  
306 approximation, the simulations with the Tillotson EOS may provide less reliable temperatures than  
307 with ANEOS, which directly relates the temperature to the other quantities.

308 During crater formation ( $t = 1 \mu\text{s}$ , Fig. 6A-B), a  $>2$ -mm heated zone surrounds the crater.  
309 In particular, the temperature of the upper half layer of the heated zone exceeds  $\sim 2600^\circ\text{C}$ , the  
310 liquidus for iron at pressures  $\sim 70 \text{ GPa}$  (maximum pressure in the target; Ahrens et al., 1998). This  
311 confirms that liquid metal is formed during the impact, as expected from the presence of spheroidal  
312 metal blebs in crater and ejecta (Ganino et al., 2018), or by metal-silicate liquid immiscibility in

313 craters (Libourel et al., 2019). At the end of the simulation when the crater is in steady state ( $t =$   
314  $10 \mu\text{s}$ , Fig. 6C-D), a zone heated above  $100^\circ\text{C}$  remains between 1 and  $\sim 3$  mm (on the sides and  
315 below the crater, respectively). The maximum temperatures are reached in the uppermost layer in  
316 the crater, which is right at the liquidus temperature for SCM 435 steel at room pressure ( $\sim 1500^\circ\text{C}$ )  
317 and therefore could still contain melted residues. Remarkably, the temperatures both at  $1 \mu\text{s}$  and  
318  $10 \mu\text{s}$  do not drastically differ between the case with the Tillotson EOS and ANEOS. In our case,  
319 the Tillotson EOS seems to provide a relatively reliable approximation of the temperature in the  
320 target. In both cases, we suspect that the highest temperatures ( $\gg 2600^\circ\text{C}$ ) could be artifacts due  
321 to the still relatively coarse resolution of the simulations. Note that the Tillotson EOS has a  
322 continuous analytic solution for internal energy (and therefore temperature), whereas for ANEOS,  
323 a grid of temperatures accessible to the EOS must be created. This is due to the fact that Spheral++  
324 evolves the model in terms of the specific thermal energy, while ANEOS works in temperature.  
325 For efficiency, Spheral++ accommodates this difference by computing lookup tables converting  
326 the energy to temperature (as a function of density) and using bilinear interpolation to go between  
327 the two. This increases the computation speed at the expense of a certain discreteness in the  
328 resulting temperatures. In the simulations, the resolution for the ANEOS case was  $\sim 50^\circ\text{C}$ , which  
329 explains why small temperature differences cannot be resolved (Fig. 6A-D).

330

## 331 **5. Discussion**

### 332 **5.1. Tillotson EOS versus ANEOS**

333 Overall, in the conditions of the experiment we replicated, the influence of the EOS on the  
334 outcomes of the simulations remains limited and always depends on other parameters such as the  
335 initial flaw distribution. In terms of crater dimensions, ANEOS cases are overall closer to the

336 experimental values than the Tillotson cases. However, for the Weibull shape parameter  $m = 8$   
337 found in the literature (Asphaug et al., 2002) and reasonable values of the scale parameter  $\sigma_N$  (0.8–  
338 0.9 GPa) estimated by simple calculation (Section 2.3) both EOS yield accurate dimensions. In  
339 terms of temperature recorded in the target, we do not find a significant difference between ANEOS  
340 and the Tillotson EOS, which in this case provides reliable temperature estimates despite the  
341 approximation of a constant specific heat capacity. Finally, except for extreme values of the  
342 Weibull scale parameter  $\sigma_N < 0.2$  GPa where the target fails with ANEOS but is only widely  
343 damaged with Tillotson, there is no notable difference in the amount of material damaged between  
344 the two EOS. The simulations with ANEOS globally result in a damage ~10% higher than with  
345 Tillotson, though in both cases the target is only marginally affected (damage below 40%).

346

## 347 **5.2. Steel versus meteoritic metal**

348 Iron meteorites—possible analog to Psyche’s surface material—are made of a Fe-Ni alloy that was  
349 most often very slowly cooled (a few degrees per million years), yielding the formation of very  
350 specific structures characteristic of meteoritic alloys. One of the most striking example is the  
351 formation of the Widmanstätten pattern, a mm-scale intergrowth of two Fe-Ni phases called  
352 kamacite (Ni-poor) and taenite (Ni-rich) that gives iron meteorites their recognizable geometric  
353 pattern when etched (Buchwald, 1975). With such exceptional cooling conditions and resulting  
354 heterogeneities, differences may be expected between the mechanical behavior of iron meteorites  
355 and that of man-made steels. The limited number of impact experiments and strength tests carried  
356 out on iron meteorites had companion experiments made on various steel targets (Matsui and  
357 Schultz, 1984; Katsura et al., 2011; Ogawa et al., 2017; Libourel et al. 2019). Tensile tests carried  
358 out on the iron meteorite Gibeon measured a yield strength at room temperature of ~310 MPa  
359 (Johnson and Remo, 1974), similar to that of the SCM 435 steel (~350 MPa). Matsui et al. (1984)

360 performed high-velocity impact experiments on 1020 steel (yield strength ~300 MPa), pure iron  
361 and three iron meteorites. They found that crater size and shape (lip) were very similar for each  
362 type of target. Matsui et al. (1984) also reported evidence of failure on most iron meteorites, with  
363 cracks propagating along the Widmanstätten discontinuities. Similar observations (lip and cracks  
364 along boundaries) were made by Libourel et al. (2019) after comparison between impacts on  
365 Gibeon and on SCM 435 steel. This difference likely emerges from the contrast between a  
366 relatively isotropic steel and highly anisotropic iron meteorites. The similarities between the craters  
367 in steel and in meteorite show the relevance of modeling steel targets, for which more data are  
368 available. On the other hand, the failure observed on meteorites away from the crater suggests that  
369 the Weibull distribution for incipient flaws may have to be adapted for iron meteorites and should  
370 not necessarily be assumed to be similar to steel, because of the weaker interfaces of the meteoritic  
371 Widmanstätten structure. However, whether such heterogeneities are relevant for planetary-scale  
372 impacts remains to be investigated.

373

### 374 **5.3. Possible implications for impact craters on Psyche**

375 The results of our simulations allow us to compare and contrast what impacts into targets of  
376 different compositions might be like. For a given set of initial conditions, iron targets are almost  
377 never fully damaged but rather experience a minor and very localized weakening, whereas a  
378 basaltic target is more widely weakened. Crater size gives us another way to examine these trends.  
379 In the experiment simulated here, the crater to projectile diameter ratio is 2.6 (and varies between  
380 2.2 and 2.9 for other experiments conducted by Ganino et al. (2018) for velocities between 3.39  
381 and 6.88 km s<sup>-1</sup>). In comparison, impacts at 6.9 km s<sup>-1</sup> into aluminum targets yield a ratio of 4.8  
382 (Hörz, 2012). Both these values are smaller than the value of 8 calculated from scaling laws for  
383 intact basalt (Holsapple and Housen, 2007; Marchi et al., 2010).

384           Scaling laws tested against experiments on silicate targets predict that the threshold for  
385 catastrophically destroying the target, and therefore activating flaws, will decrease as the target's  
386 size increases (Housen and Holsapple, 1999). This dependence is in particular controlled by the  
387 shape parameter  $m$ . Since the value of this parameter estimated in this study ( $m = 8\text{--}10$ ) bracket  
388 that estimated for basalt ( $m \sim 9.5$ ), it is expected that, like a silicate object, an iron-rich object of  
389 increasing size will get weaker.

390           However, in the case of cratering, we have seen that the strength of the target influences the  
391 crater size. Therefore, despite the fact that both silicate-rich and metal-rich targets would weaken  
392 at larger scale, the threshold for failure for iron will always be higher than that for silicate. The  
393 implication is that for equivalent impacts, much larger or faster projectiles would be necessary to  
394 cause a similar crater on a metal-rich surface as that inflicted to a silicate one. As a consequence, a  
395 comparison between impact experiments or simulations and the size-frequency distribution of  
396 craters measured on Psyche combined with models of the main belt population may allow us to  
397 glean insights into the composition and strength of Psyche's surface relative to other asteroid  
398 surfaces. A different crater to projectile diameter ratio on Psyche than that measured on other main  
399 belt asteroids would also mean that scaling laws derived for objects dominated by silicates could  
400 not optimally apply to this asteroid.

401           This study focused on modeling non-porous, pure-iron targets. It is probable that Psyche's  
402 surface and subsurface will rather be made of a mixture of iron with silicates, possibly hydrated  
403 (Takir et al., 2017), and possibly micro or macroporous. Moreover, we only focused on vertical  
404 impacts, even though oblique impacts would more realistically occur in nature (Pierazzo and  
405 Melosh, 2000). With confidence that vertical impacts on pure iron can be well replicated, a next  
406 step could be to introduce complexities such as oblique impacts, along with varying microporosity  
407 and macroporosity of the target. Further simulating layered or rubble-pile-like silicate-iron

408 mixtures, in comparison with experiments on stony-iron meteorites and alloyed mixtures, will  
409 allow us to explore the effects of surface heterogeneities on the fate of impact craters.

410

## 411 **6. Conclusion**

412 Understanding the outcomes of impact processes on iron alloys and iron meteorites, as well as their  
413 scaling to planetary-like events is crucial for the optimal interpretation of the cratering data of the  
414 forthcoming NASA Discovery mission Psyche. Moreover, verifying the reliability of numerical  
415 models applicable to metals against simple experiments is an essential step toward more general  
416 investigations of planetary processes involving metallic or differentiated bodies. This work aims at  
417 better characterizing the influence of numerical parameters in the modeling of high-velocity  
418 impacts in steel targets, and possibly iron meteorites, using the ASPH package Spheral++. For a  
419 given strength model of stainless steel, we investigated the influence of the equations of state  
420 (Tillotson EOS and ANEOS), as well the influence of the Weibull distribution of incipient flaws  
421 in the material. The crater dimensions are within 10% of the experimental value in more cases with  
422 ANEOS than the Tillotson EOS. However, for reasonable Weibull parameters estimated from the  
423 literature or simple calculations, both EOS yield craters similar to the experimental one. In a  
424 majority of cases and independently from the EOS, the target does not fail and is only marginally  
425 damaged (damage <40% within 1 to 2 mm around the crater). Finally, the recorded temperatures  
426 are not significantly affected by the choice of the EOS and reach locally values above the melting  
427 point of iron at pressure <100 GPa, which is in good agreement with experimental observations of  
428 melted metal beads coming from the target. This work highlights the importance of specifically  
429 studying impacts in Psyche-like targets, because crater formation differs from what would be  
430 observed with a silicate target in similar impact conditions. Differences might therefore be expected

431 between the crater size distribution of Psyche (if metal is dominating the surface and subsurface)  
432 and other asteroids of similar size orbiting in the main belt. The NASA Psyche mission will for the  
433 first time image impact craters on a metal-rich asteroid and predictions arising from experimental  
434 and numerical work will be valuable during data interpretation.

435

## 436 **Acknowledgements**

437 We are very grateful to Dr. Dawn Graninger for her help with the ANEOS package in Spheral++,  
438 and to Dr. William F. Bottke and Dr. Simone Marchi for their comments on the manuscript. The  
439 simulations presented in this paper were performed on the Engaging cluster located at the  
440 Massachusetts Green High Performance Computing Center (MGHPCC). C.M. thanks the NASA  
441 Discovery program (Psyche mission) for financial support. P.M. acknowledges funding support  
442 from the French space agency CNES and from Academies of Excellence: Complex systems and  
443 Space, environment, risk, and resilience, part of the IDEX JEDI of the Université Côte d'Azur. The  
444 work of M.B.S. and J.M.O. was performed under the auspices of the U.S. Department of Energy  
445 by Lawrence Livermore National Laboratory under Contract DE-AC52-07NA27344.

446

## 447 **References**

448 Ahrens, T. J., Holland, K. G. and Chen, G. Q. (1998) Shock temperatures and the melting point of  
449 iron, AIP Conference Proceedings 429, 133–136.

450

451 Asphaug, E. and Reufer A. (2014) Mercury and other iron-rich planetary bodies as relics of  
452 inefficient accretion, Nat. Geosci. **7**, 564–567.

453

454 Asphaug, E., Ryan, E. V. and Zuber, M. T. (2002) Asteroid interiors, in Bottke et al. Eds., Asteroid  
455 III, pp. 463–484.  
456

457 Benz, W. and Asphaug E. (1994) Impact simulations with fracture. I. Method and tests, *Icarus* **107**,  
458 98–116.  
459

460 Bergman, B. (1985) On the variability of the fracture stress of brittle materials, *J. Mater. Sci. Lett.*  
461 **4**, 1143–1146.  
462

463 Buchwald, V. F. (1975) *Handbook of iron meteorites*, Vol. 1, 254 pp.  
464

465 Collins, G. S., Melosh, H. J. and Ivanov, B. A. (2004) Modeling damage and deformation in impact  
466 simulations, *Meteorit. Planet. Sci.* 39, 217–231.  
467

468 Elkins-Tanton, L. T., Asphaug, E., Bell, J. F., et al. (2017) Asteroid (16) Psyche: visiting a metal  
469 world, abstract 1718, 48th Lunar and Planetary Sci. Conf., The Woodlands, TX, March 20–24,  
470 2017.  
471

472 Ganino, C., Libourel, G., Nakamura, A. M., Jacomet, S., Tottereau, O. and Michel, P. (2018)  
473 Impact-induced chemical fractionation as inferred from hypervelocity impact experiments with  
474 silicate projectiles and metallic targets, *Meteorit. Planet. Sci.* 53, 2306–2326.  
475

476 Grady, D. E. (2003) Investigation of explosively driven fragmentation of metals-two-dimensional  
477 fracture and fragmentation of metal shells: progress report II, doi:10.2172/15005042.

478

479 Grady, D. E. and Kipp, M. E. (1980) Continuum modelling of explosive fracture in oil shale, *Int.*  
480 *J. Rock Mech. Min. Sci. & Geomech. Abstr.* **17**, 147–157.

481

482 Holsapple, K. A. and Housen, K. R. (2007) A crater and its ejecta: An interpretation of Deep  
483 Impact, *Icarus* **191**, 586–597.

484

485 Hörz, F. (2012) Cratering and penetration experiments in aluminum and teflon: Implications for  
486 space-exposed surfaces, *Met. Planet. Sci.* **47**, 763–797.

487

488 Housen, K. R. and Holsapple, K. A. (1999) Scale effects in strength-dominated collisions of rocky  
489 asteroids, *Icarus* **142**, 21–33.

490

491 Johnson, G. R. and Cook, W. H. (1985) Fracture characteristics of three metals subjected to various  
492 strains, strain rates, temperatures and pressures, *Eng. Fract. Mech.* **21**, 31–48.

493

494 Johnson, A. A. and Remo, J. L. (1974) A new interpretation of the mechanical properties of the  
495 Gibeon meteorite, *J. Geophys. Res.* **79**, 1142–1146.

496

497 Jutzi, M., Holsapple, K., Wünneman, K. and Michel P. (2015) Modeling asteroid collisions and  
498 impact processes, in Michel et al. Eds., *Asteroid IV*, pp. 679–699.

499

500 Katsura, T., Nakamura A. M., Takabe, A., Okamoto, T., Sange, K., Hasegawa, S., Liu, X. and  
501 Mashimo, T. (2011) Impact experiments on collisional evolution of iron regolith, abstract 1695,  
502 42nd Lunar and Planetary Sci. Conf., The Woodlands, TX, March 7–11.

503  
504 Kraus, R. G., Root, S., Lemke, R. W., Stewart, S. T., Jacobsen, S. B. and Mattsson, T.R. (2015)  
505 Impact vaporization of planetesimal cores in the late stages of planet formation, *Nat. Geosci.*  
506 **8**, 269–272.

507  
508 Libourel, G., Nakamura, A. M., Beck, P., Potin, S., Ganino, C., Jacomet, S., Ogawa, R., Hasegawa,  
509 S., Michel, P. (2019) Hypervelocity impacts as a source of deceiving surface signatures on iron-  
510 rich asteroids, *Sci. Adv.* **5**, eaav3971.

511  
512 Marchi, S., Barbieri, C., Küppers, M., Marzari, F., Davidsson, B., Keller, H. U., Besse, S., Lamy,  
513 P., Mottola, S., Massironi, M. and Cremonese, G. (2010) The cratering history of asteroid (2867)  
514 Steins, *Planet. Space Sci.* **58**, 1116–1123.

515  
516 Marchi, S., Durda, D. D., Polanskey, C. A., Asphaug, E., Bottke, W. F., Elkins-Tanton, L. T.,  
517 Garvie, L. A. J., Ray, S. and Williams, D. A. (2019) Hypervelocity impact experiments in metallic  
518 targets: Implications for the NASA Psyche mission, submitted to *J. Geophys. Res.*

519  
520 Marchi, S., Ermakov, A. I., Raymond, C. A. et al. (2016) The missing large impact craters on Ceres,  
521 *Nat. Commun.* **7**, 12257.

522

523 Matsui, T. and Schultz, P. H. (1984) On the brittle-ductile behavior of iron meteorites' new  
524 experimental constraints, *J. Geophys. Res.* **89**, C323–C328.

525  
526 Melosh, H. J. (1989) *Impact cratering: a geologic process*, Research supported by NASA. New  
527 York, Oxford University Press (Oxford Monographs on Geology and Geophysics, No. 11), pp.  
528 234.

529  
530 Melosh, H. J. (2007) A hydrocode equation of state for SiO<sub>2</sub>, *Meteorit. Planet. Sci.* **42**, 2079–2098.

531  
532 Melosh, H. J., Ryan, E. V. and Asphaug, E. (1992) Dynamic fragmentation in impacts: hydrocode  
533 simulation of laboratory impacts, *J. Geophys. Res.* **97**, 14735–14759.

534  
535 Mizutani, H., Takagi, Y. and Kawakami, S.-I. (1990) New scaling laws on impact fragmentation,  
536 *Icarus* **87**, 307–326.

537  
538 Monaghan, J. J. (1992) Smoothed particles hydrodynamics, *Annu. Rev. Astron. Astr.* **30**, 543–574.

539  
540 Nakamura, A. M., Michel, P. and Sehto, M. (2007) Weibull parameters of Yakuno basalt targets  
541 used in documented high-velocity impact experiments, *J. Geophys. Res.* **112**, E02001.

542  
543 Nesterenko, V. F. (2001) *Dynamics of heterogeneous materials*, Springer-Verlag New York, pp.  
544 177.

545

546 Neukum, G., Ivanov, B. A. and Hartmann, W. K. (2001) Cratering records in the inner solar system  
547 in relation to the lunar reference system, *Space Sci. Rev.* **96**, 55–86.  
548

549 Ogawa, R., Nakamura, M. and Hasegawa, S. (2017) The effect of temperature and impact velocity  
550 on crater shape on the surface of iron bodies, abstract 6074, 80th Annual Meeting of the  
551 Meteoritical Society, Santa Fe, NM, June 23–28.  
552

553 Owen, J. M. (2004) A tensor artificial viscosity for SPH, *J. Comput. Phys.* **201**, 601–629.  
554

555 Owen, J. M. (2014) A compatibly differenced total energy conserving form of SPH, *Int. J. Numer.*  
556 *Meth. Fluids* **75**, 749–775.  
557

558 Owen, J. M., Villumsen, J. V., Shapiro, P. R. and Martel, H. (1998) Adaptive smoothed particle  
559 hydrodynamics: Methodology. II, *Astrophys. J. Suppl. Ser.* **116**, 155–209.  
560

561 Pierazzo, E. and Melosh, H. J. (2000) Understanding oblique impacts from experiments,  
562 observations, and modeling, *Annu. Rev. Earth Planet. Sci.* **28**, 141–167.  
563

564 Shapiro, P. R., Martel, H., Villumsen, J. V. and Owen, J. M. (1996) Adaptive smoothed particle  
565 hydrodynamics, with application to cosmology: Methodology, *Astrophys. J. Suppl. Ser.* **103**, 269–  
566 330.  
567

568 Shepard, M. K., Richardson, J., Taylor, P. A., et al. (2017) Radar observations and shape model of  
569 asteroid 16 Psyche, *Icarus* **281**, 388–403.

570

571 Steinberg, D. J., Cochran, S. G. and Guinan, M. W. (1980) A constitutive model for metals  
572 applicable at high-strain rate, *J. Appl. Phys.* **51**, 1498–1504.

573

574 Takir, D., Reddy, V., Sanchez, J. A. , Shepard, M. K. and Emery, J.P. (2017) Detection of water  
575 and/or hydroxyl on asteroid (16) Psyche, *Astronomical Journal* **153**:31.

576

577 Thompson, S. L. (1990) ANEOS analytic equation of state for shock physics codes input manual.  
578 Sandia National Laboratory Report SAND89-2951.

579

580 Thompson, S. L. and Lauson, H. S. (1972) Improvements in the Chart D radiation-hydrodynamic  
581 CODE III: Revised analytic equations of state, Sandia National Laboratory Report SC-RR-71 0714.

582

583 Tillotson, J. H. (1962) Metallic equation of state for hypervelocity impacts, General Atomic Report  
584 GA-3216.

585

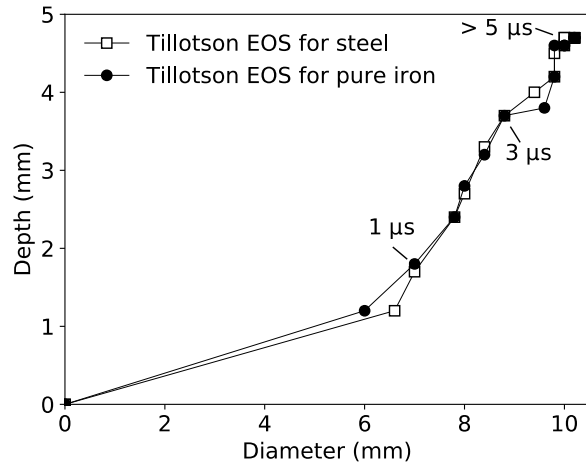
586 Viikinkoski, M., Vernazza, P., Hanuš, J., et al. (2018) (16) Psyche: A mesosiderite-like asteroid?  
587 *Astron. Astrophys.* **619**, L3.

588

589 Weisberg, M. K., Prinz, M., Clayton, R. N., Mayeda, T. K., Sugiura, N., Zashu, S. and Ebihara, M.  
590 (2010) A new metal-rich chondrite grouplet, *Meteorit. Planet. Sci.* **36**, 401–418.

591 **Figures**

592



593

594

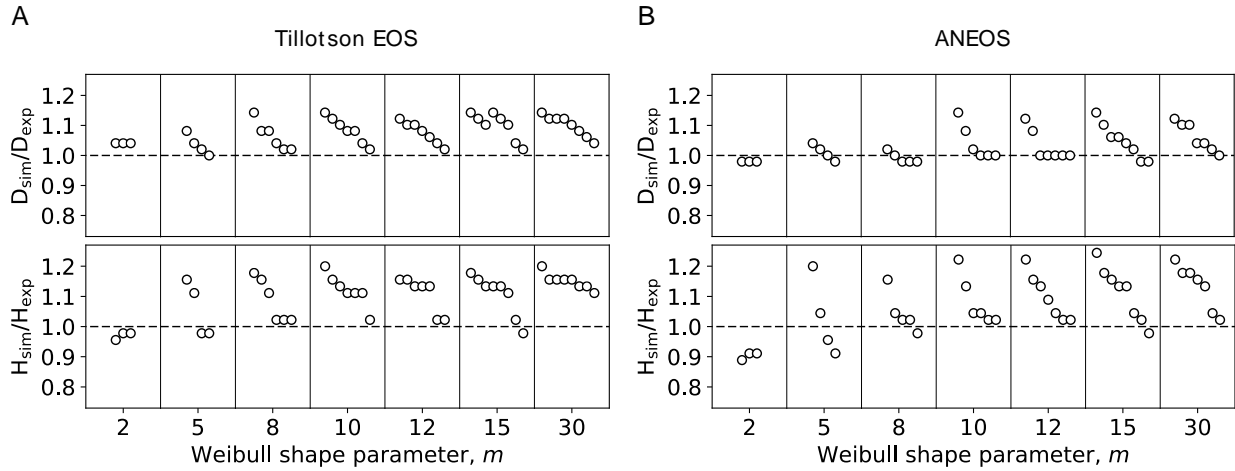
595 Fig. 1. Depth versus diameter of a crater formed after an impact at  $6.89 \text{ km s}^{-1}$  by an impactor  $\sim 1.9$ -

596 mm in radius, for two different sets of Tillotson parameters: pure iron (Melosh, 1989) and steel

597 (Nesterenko, 2001). Apart from their EOS parameters (given in Table 1), the targets were identical.

598 The simulations lasted  $10 \mu\text{s}$  and both craters had their final shape at the end of the simulation.

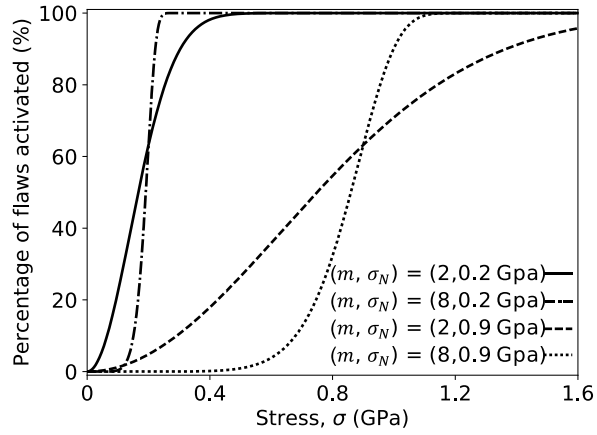
599 Squares and circles represents  $0.5\text{-}\mu\text{s}$  time steps.



600

601

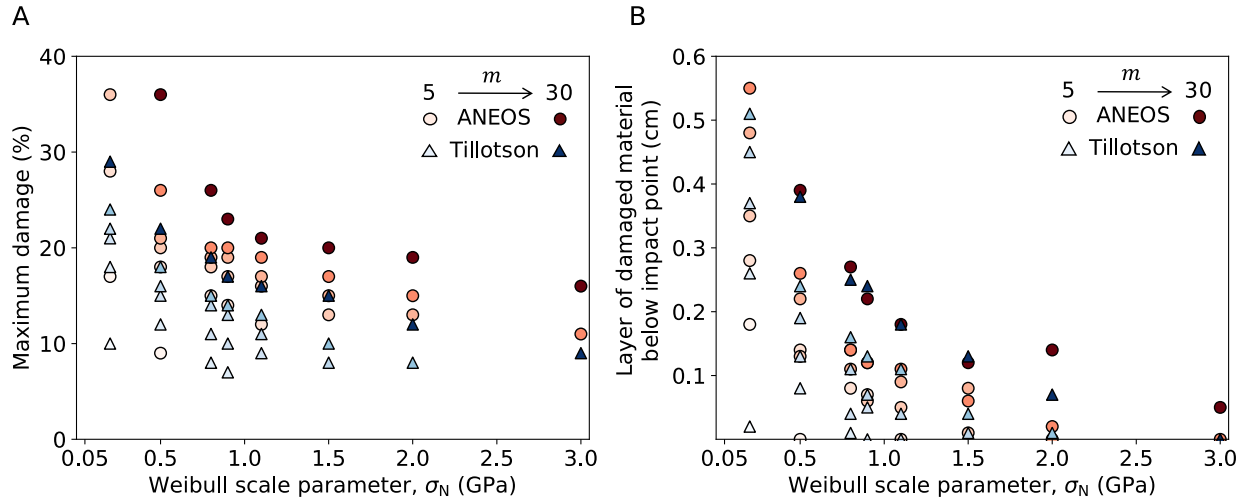
602 Fig. 2. Crater dimensions as a function of the Weibull shape parameter  $m$  for the simulations with  
 603 the Tillotson EOS (A) and ANEOS (B). Each rectangle represents one value of  $m$  and white dots  
 604 represent increasing values of  $\sigma_N$  (see Table 3) from left to right. The top panels show the diameter  
 605 of the crater ( $D_{sim}$ ) normalized by the experimental value ( $D_{exp} = 9.8$  mm) and the bottom panels  
 606 show the depth of the crater ( $H_{sim}$ ) normalized by the experimental value ( $H_{exp} = 4.5$  mm). The grey  
 607 bands highlight the dimensions that are within  $\pm 10\%$  of the experimental values.



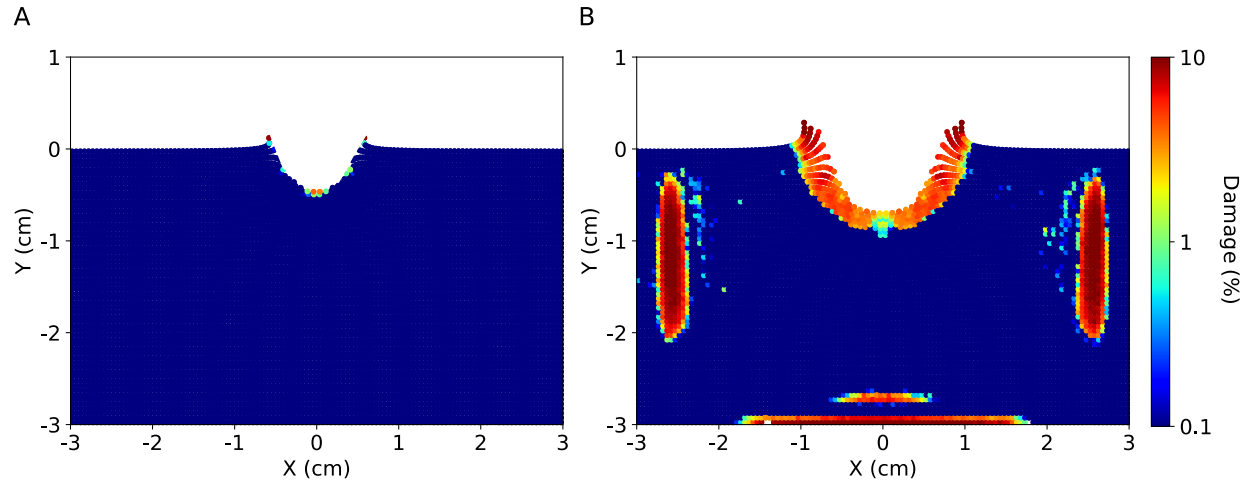
608

609 Fig. 3. Percentage of activated flaws as a function of stress, assuming a Weibull distribution with

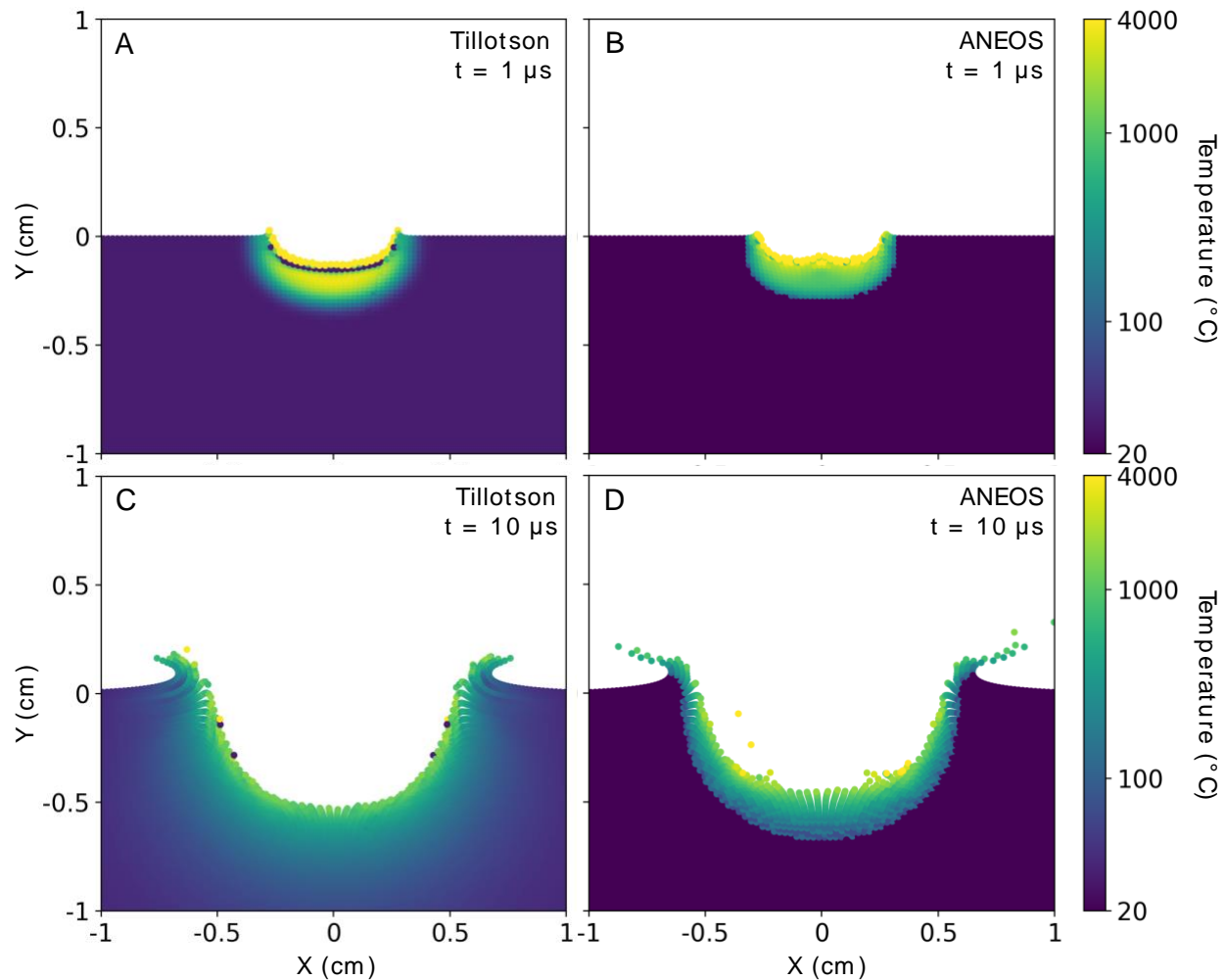
610 shape parameter  $m = 2$  or  $8$ , and scale parameter  $\sigma_N = 0.2$  or  $0.9$  GPa.



611  
 612  
 613 Fig. 4. A) Maximum damage (in %) reached in a node of the target (typically near the impact point)  
 614 as a function of the Weibull scale parameter  $\sigma_N$ . This does not account for ejected material. Circles  
 615 and triangles represent the simulations with ANEOS and the Tillotson EOS, respectively. The  
 616 increasing color darkness corresponds to increasing values of  $m$ . The cases with zero or full damage  
 617 are not included. B) Thickness of the layer below the impact point with non-zero damage as a  
 618 function of the Weibull scale parameter  $\sigma_N$ .



619  
 620 Fig. 5. A) Damage in the steel target at the end of the simulation ( $10 \mu\text{s}$ ) obtained with the Weibull  
 621 parameters  $(m, \sigma_N) = (8, 0.9 \text{ GPa})$ . B) Damage in a basalt target with otherwise identical impact  
 622 conditions. The color bar applies to both panels and correspond to the maximum eigenvalue of the  
 623 damage tensor. The damage of the steel target is minor and very localized at the bottom of the  
 624 crater compared to the damage of basalt target. Conversely to the crater in steel, the crater in basalt  
 625 is still mildly expanding at  $10 \mu\text{s}$ .



626

627

628 Fig. 6. Temperature in the target after 1  $\mu\text{s}$  (A-B) and 10  $\mu\text{s}$  (C-D). Simulations use the Tillotson

629 EOS (A-C) and ANEOS (B-D) with Weibull parameters  $(m, \sigma_N) = (8, 0.9 \text{ GPa})$  and a resolution

630 of 0.2 mm.

631 **Tables**

632

<b>Parameter</b>	<b><i>a</i></b>	<b><i>b</i></b>	<b><i>A</i></b> <b>(GPa)</b>	<b><i>B</i></b> <b>(GPa)</b>	<b><i>E</i><sub>0</sub></b> <b>(J kg<sup>-1</sup>)</b>	<b><i>α</i></b>	<b><i>β</i></b>	<b><i>E</i><sub>IV</sub></b> <b>(J kg<sup>-1</sup>)</b>	<b><i>E</i><sub>CV</sub></b> <b>(J kg<sup>-1</sup>)</b>
<b>Pure iron</b>	0.5	1.5	128	105	9.5×10 <sup>6</sup>	5	5	2.4×10 <sup>6</sup>	8.67×10 <sup>6</sup>
<b>Steel</b>	0.55	0.62	117	55	17.5×10 <sup>6</sup>	5	5	2.4×10 <sup>6</sup>	8.67×10 <sup>6</sup>

633

634 Table 1. Tillotson parameters published for pure iron (Melosh, 1989) and steel (Nesterenko, 2001).

635 Parameters *a*, *b*, *A*, *B*, *E*<sub>0</sub> are material-specific, *α*, *β* are fitting parameters and *E*<sub>IV</sub>, *E*<sub>CV</sub> are the636 energy of incipient and complete vaporization, respectively. Because the values of *E*<sub>IV</sub> and *E*<sub>CV</sub> for

637 steel were not provided by Nesterenko (2001), we used the same values as pure iron.

<b>Parameter</b>	<b><math>G_0</math> (MPa)</b>	<b><math>Y_0</math> (MPa)</b>	<b><math>A</math> (MPa<sup>-1</sup>)</b>	<b><math>B</math> (K<sup>-1</sup>)</b>	<b><math>\beta</math></b>	<b><math>n</math></b>	<b><math>Y_{\max}</math></b>
<b>Stainless steel (except <math>Y_0</math>)</b>	$7.7 \times 10^5$	350	$2.26 \times 10^{-6}$	$4.55 \times 10^{-4}$	43	0.35	$2.5 \times 10^3$

638

639 Table 2. Parameters of the Steinberg-Guinan strength model for stainless steel (Steinberg et al.,

640 1980).  $Y_0$  is taken equal to the yield strength of the SCM 435 steel used in the experiment.

$k$ (cm <sup>-3</sup> )		Shape parameter $m$						
		2	5	8	10	12	15	30
Scale parameter $\sigma_N$ (GPa)	0.05	1.41e5	9.05e15	5.79e26	9.27e33	1.5e41		
	0.2	8.84e3	8.84e12	8.84e21	8.87e27	9.2e33	9.2e42	9.2e87
	0.5	1.41e3	9.05e10	5.79e18	9.27e23	1.48e29	9.49e36	1.1e76
	0.8		8.63e9	1.34e17	8.43e21	5.27e26	8.23e33	8.0e69
	0.9			5.25e16	2.59e21	1.28e26	1.40e33	2.4e68
	1.1			1.06e16	3.49e20	1.15e25	6.93e31	5.44e65
	1.5				1.57e19	2.9e23	6.61e29	4.95e61
	2.0					8.84e21	8.84e27	8.84e57
	3.0						2.02e25	4.61e52

641  
642 Table 3. Corresponding values of the Weibull parameter  $k$  for a given shape parameter  $m$  and scale  
643 parameter  $\sigma_N$ . The combinations showed with a gray cell were not investigated. These values were  
644 obtained using the equation  $k = 1/V(E/\sigma_N)^m$  (Nakamura et al., 2007), where  $V$  is the volume of  
645 the target (108 cm<sup>3</sup> in the simulations) and  $E$  the Young modulus of the target material (~200 GPa).